Rare Metal Materials and Engineering
Volume 51, Issue 2, February 2022
Available online at www.rmme.ac.cn

Science Press

Cite this article as: He Junguang, Xu Dazhao, Wen Jiuba, et al. Microstructure, Mechanical Properties and Corrosion Behavior of Biodegradable As-extruded Mg-2Zn-1Y-0.5Zr Alloys[J]. Rare Metal Materials and Engineering, 2022, 51(02): 474-483.

ARTICLE

Microstructure, Mechanical Properties and Corrosion Behavior of Biodegradable As-extruded Mg-2Zn-1Y-0.5Zr Alloys

He Junguang[1,2], Xu Dazhao[2], Wen Jiuba[1,2], Shi Huina[1], Wang Yangfan[3], Ren Xiaolei[4]

[1] School of Materials Science and Engineering, Henan University of Science and Technology, Luoyang 471023, China; [2] Collaborative Innovation Center of Nonferrous Metals, Luoyang 471023, China; [3] Wenzhou University, Wenzhou 325000, China; [4] Dalian University of Technology, Dalian 116024, China

Abstract: The effects of extrusion temperature on dynamic recrystallization, texture and tensile properties of biodegradable Mg-2Zn-1Y-0.5Zr alloys were studied, and the corrosion mechanisms of as-extruded alloys in SBF solution were elaborated. The results show that the extruded alloy at 440 ℃ (E440) has a bimodal structure with coarse unrecrystallized (unDRXed) grains and fine recrystallized (DRXed) grains. The deformed grains from unDRXed region make the greatest contribution to the texture strength. The extruded alloy at 460 ℃ (E460) has uniform DRXed grains, and its excellent tensile properties reveal a dominance of fine grain strengthening. Simultaneously, the uniform DRXed grains are good for the weakening of texture strength. The E460 sample exhibits the best corrosion resistance with a corrosion rate of 0.669 ± 0.017 mm·a^{-1}.

Key words: biodegradable; extrusion; recrystallization; corrosion behavior

Biodegradable magnesium alloys have received extensive attention due to their excellent biocompatibility[1-3]. Magnesium alloys can lessen the stress shielding effect because of their certain characteristics (density and elastic modulus) close to human bone[4, 5]. Magnesium takes part in human metabolism and simulates the growth of new bones[6]. In addition, degradable magnesium alloys do not need follow-up surgery to remove implants, which can avoid the risk of secondary surgery[1]. However, poor mechanical properties and rapid degradation rate prevent them from being widely applied for the loss of mechanical integrity during implantation[7-9].

Micro-alloying can significantly promote the overall performance of biodegradable magnesium alloys[10]. Suitable alloying elements should be selected. The content of corresponding alloying elements should be controlled within a certain safe range. Zinc (Zn) is a human nutrient. Adding proper content of Zn into magnesium alloy can strengthen its strength and corrosion resistance[11]. Zirconium (Zr) is a common and effective grain refiner in magnesium alloys. Adding less than 2% Zr to magnesium alloy can improve its comprehensive performance[3]. In addition, rare-earth (RE) elements can be used in biomedical materials, while the toxicity of it should be considered. Studies show that magnesium alloys with low content RE element Y do not exhibit cell toxicity[12, 13]. Besides, He et al [14] believed that adding Y into magnesium alloy can promote the biological corrosion performance. Liu et al [15] concluded that the addition of right amount of Y can greatly improve the corrosion resistance. Though micro-alloying can improve the overall behavior, the mechanical characters of most casting alloys cannot meet the requirements of biomaterials. Strong texture will be formed in the process of hot deformation of non-RE Mg alloys. The addition of RE elements can effectively reduce the texture strength of Mg alloys[16,17]. In addition, the texture strength also depends on the recrystallization after plastic deformation. The recrystallized grains with random orientation can weaken the texture

Received date: February 25, 2021
Foundation item: Natural Science Foundation of Henan Province, China (162300410213)
Corresponding author: He Junguang, Ph. D., Associate Professor, School of Materials Science and Engineering; Henan University of Science and Technology, Luoyang 471023, P. R. China, E-mail: he.ellen@163.com

strength, and the subsequent growth of recrystallized grains will also affect the texture[18]. For RE-containing Mg alloys, proper thermal deformation can effectively promote their strength and corrosion behavior[19]. Xu et al[20] found that the extruded Mg-Zn-Y-Gd-Zr alloy has fine grains and uniform microstructure, showing better corrosion resistance. Mostaed et al [21] found that ZK60 alloys have fine grains after ECAP treatment, and the mechanical characters and corrosion performance are greatly improved. Zhang et al [22] found that the extruded JDBM alloy exhibits good biological corrosion performance, and JDBM shows uniform corrosion morphology in SBF.

In this work, Mg-2Zn-1Y-0.5Zr alloys were treated by hot extrusion. According to the previous research[23-25] of our team and several experiments of Mg-2Zn-1Y-0.5Zr alloys extrusion temperature, three pre-heating temperatures had been determined, namely: 440, 460, and 500 °C. The effects of extrusion temperature on dynamic recrystallization, texture and tensile properties of Mg-2Zn-1Y-0.5Zr alloy were studied. The corrosion mechanisms of as-extruded alloys in SBF solution were elaborated as well.

1 Material and Methods

1.1 Material preparation

In this study, nominal component Mg-2Zn-1Y-0.5Zr (wt%) alloys (determined as Mg-2.14Zn-0.79Y-0.24Zr by XRF) were employed. The as-cast alloys were denoted as ZWK210 alloys for simplification. The casting process was in our previous work[26]. The ingots were homogenized at 440 °C for 10 h and then quenched at 65 °C water. Homogenized samples for extrusion were processed into cylindrical ingots of Φ49 mm× 40 mm, followed by preheating at different temperatures of 440, 460 and 500 °C for 2 h; subsequently, they were hot extruded and then cooled to ambient air temperature; these extruded samples were denoted as E440, E460 and E500, respectively. The extrusion ratio was about 7.7: 1 and the extrusion speed was 5 mm/s.

1.2 Microstructure characterization

Microstructure characterization and phase analysis were performed via optical microscopy (OM, OLYMPUS), field emission scanning electron microscopy (FESEM, JSM-7800F), electron backscatter diffraction (EBSD), X-ray diffractometer (XRD) and transmission electron microscopy (TEM, JEM-2010).

1.3 Biodegradation properties

The immersion test was performed in the simulated body fluid (SBF) for 120 h. The size of immersion sample was Φ18 mm×3 mm, and the ratio of SBF solution volume to the sample surface area was 30 mL: 1 cm^2 (based on ASTM G31-72)[20]. Change SBF every 24 h to keep pH relatively stable, and keep SBF at 37±0.5 °C[27]. Use ultrasonic waves to clean the corrosion products in a boiling chromic acid solution[28]. After removing corrosion products, three-dimensional morphology of the corroded surface was analyzed by laser scanning confocal microscopy (LSCM, LEXT-OLS4100). The calculation method of corrosion rate is referred to Ref. [28]. The results of the three control groups were averaged.

The electrochemical test was performed on the electrochemical workstation (Autolab PGSTAT128N). Electrochemical specimens were mechanically polished before testing (exposed area of 1 cm^2). An open-circuit potential (OCP) test was conducted for 1 h and the initial condition was stable. Electrochemical impedance spectroscopy (EIS) was performed in the frequency range from 100 kHz to 100 mHz with 10 mV of amplitude. Polarization experiments was subsequently started from -250 mV to 400 mV with reference to OCP at a scanning rate of 1 mV/s.

1.4 Tensile testing

The DNS100 testing machine was used to stretch the samples along the extrusion direction (ED) at a rate of 1.0 $mm \cdot min^{-1}$. The results of the three control groups were averaged. Scanning electron microscopy (SEM, JSM-5610LV) was used to detect the fracture morphology of tensile specimens.

2 Results

2.1 Microstructure analysis

Fig. 1 shows the microstructures of homogenized ZWK210 alloy. Fig. 1a presents optical microstructures (OM), showing that the average grain size (d) is 110 μm. Most second-phase particles are dissolved in the matrix during homogenization. However, some residual Y-rich and Zr-rich particles are still observed in Fig. 1b. Fig. 1c displays the inverse pole figure (IPF). The twins are found from IPF map. The twins provide the sites of recrystallization nucleation for the subsequent extrusion deformation. The average grain size is 108 μm from IPF map, which is consistent with the results measured from the OM. The corresponding (0001) pole figure (PF) shows the intensity of 6.6 mud (multiples of uniform density), as shown in Fig.1d, which is lower than that of non-RE Mg alloys[29, 30].

Fig. 2 displays the optical microscopy microstructure of as-extruded ZWK210 alloy. Compared with homogenized alloys, the grains of as-extruded alloys are significantly refined. The E440 sample exhibits a bimodal structure with coarse unDRXed grains and fine DRXed grains. The average grain size and DRX fraction (φ_{DRX}) are 3.4 μm and 63%, respectively. The E460 sample shows uniform fine DRXed grains with an average size of 2.8 μm and DRX fraction of 78%. With the increase of extrusion temperature, some DRXed grains of E500 sample begin to grow. The average grain size and DRX fraction are 4.9 μm and 93%, respectively. EBSD was performed to further study the impacts of extrusion temperature on microstructure.

Fig. 3a~3c show EBSD IPF maps of E440, E460 and E500 samples and Fig. 3d~3f show the corresponding PFs, respectively. Fig. 3g~3i present EBSD IPF subset maps showing grains from texture component A (Fig. 3d), texture component B (Fig. 3e) and texture component C (Fig. 3f). The E440 sample has coarse unDRXed grains and fine DRXed grains. The corresponding pole figure shows the intensity of

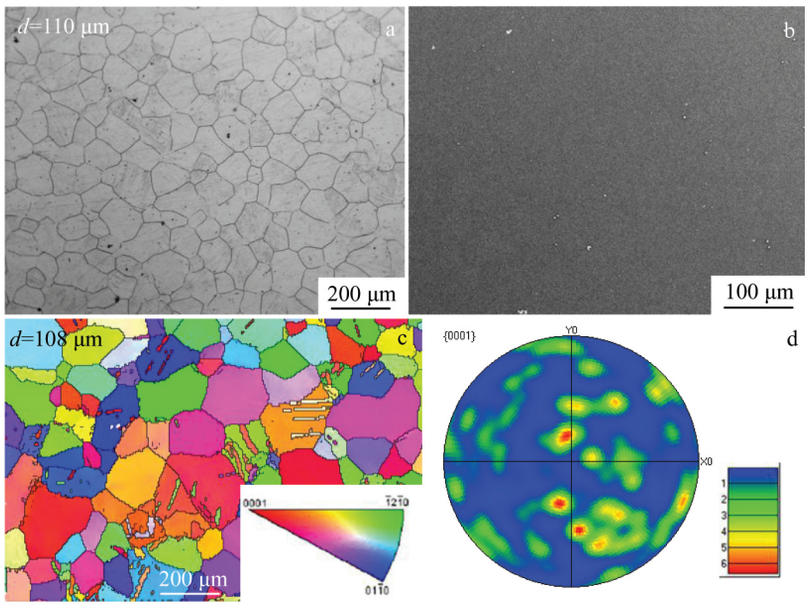

Fig.1 Microstructures of homogenized ZWK210 alloy: (a) OM, (b) SEM image, (c) EBSD IPF map, and (d) corresponding (0001) PF

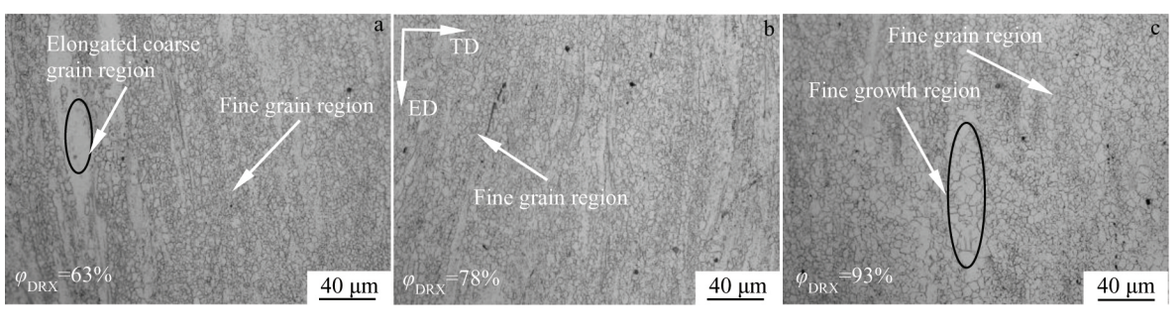

Fig.2 OM microstructures of as-extruded ZWK210 alloy: (a) E440, (b) E460, and (c) E500

31.3 mud (Fig.3f), which is much larger than that of the intial homogenized alloy (6.6 mud). The texture component A mainly originates from coarse unDRXed grains (Fig.3g). The E460 sample exhibits uniform fine DRXed grains and the corresponding pole figure shows lower intensity of 3.8 mud. The texture component B mainly comes from deformed grains (Fig. 3h). Obviously, the uniform fine DRXed grains can weaken the texture strength of Mg alloys. Some DRXed grains grow obviously in E500 sample, and an unDRXed region is observed at the same time. The texture component C mainly comes from coarse unDRXed grains and a small part of the grown DRXed grains. Compared with the texture strength of E460 sample, the corresponding pole figure of E500 sample shows lager intensity of 14.5 mud.

Fig. 4 presents the SEM images and element distribution maps. It can be seen that the particles rich in Y and Zr elements are distributed along the extrusion direction. As shown in Fig. 3a~3c, after extrusion, slender and coarse non-DRX grains appear around the densely distributed second phase particles, and the other is fine DRX grains.

Fig. 5 shows XRD pattern of E460 sample to anlyze the chemical compositions. It can be seen that the E460 sample connsists of α-Mg and $Mg_3Y_2Zn_3$. The content of $Mg_3Y_2Zn_3$ is relatively small.

To further investigate dynamic precipitates, the E460 sample was selected for TEM analysis. Fig. 6a displays a bright filed TEM image of the granular second phase, with a size of about 112 nm. The corresponding SAED patterns (Fig. 6d) indicate that the granular second phase has a face-centered cubic (fcc) structure, corresponding to the $(\bar{2}\bar{2}0)$, $(02\bar{2})$ and $(\bar{2}02\bar{2})$ faces of the $Mg_3Y_2Zn_3$ phase, with a band axis of $[\bar{1}11]$ and a lattice constant a=0.6832 nm. Therefore, the granular second phase is determined as $Mg_3Y_2Zn_3$ phase. Fig. 6b shows a bright field TEM image of the bulk second phase, with a length of about 376 nm and a width of 205 nm. According to the corresponding SAED patterns (Fig. 6e), the bulk second phase also has a fcc structure, corresponding to the $(1\bar{1}1)$, $(\bar{2}\bar{2}0)$ and $(\bar{1}\bar{3}1)$ faces of the Zn_2Zr phase, with a band axis of $[1\bar{1}2]$ and a lattice constant a=0.7395 nm. Therefore, the bulk second phase is Zn_2Zr phase. Both the granular and bulk secondary phases are inside the DRXed grains (Fig. 6c), which effectively prevent the growth of DRXed grains. A small amount of nano-sized long-rod-like second phases with a length of 300~860 nm and a width of

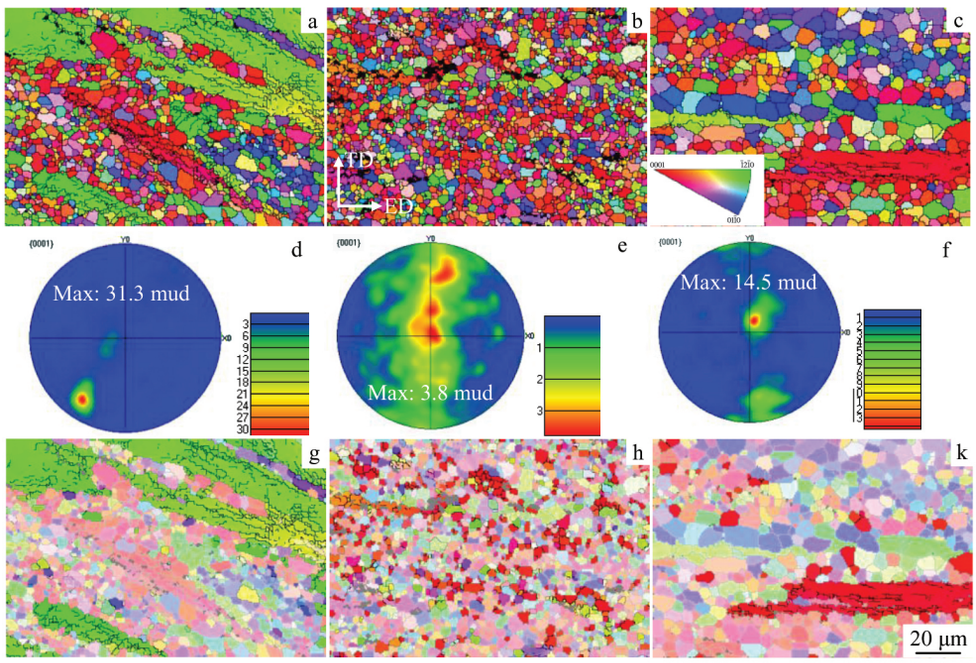

Fig.3 EBSD IPF maps (a~c) and corresponding pole figures (d~f) of E440 (a, d), E460 (b, e) and E500 (c, f); EBSD IPF subset maps showing grains from texture component A in Fig.3d (g), texture component B in Fig.3e (h) and texture component C in Fig.3f (i)

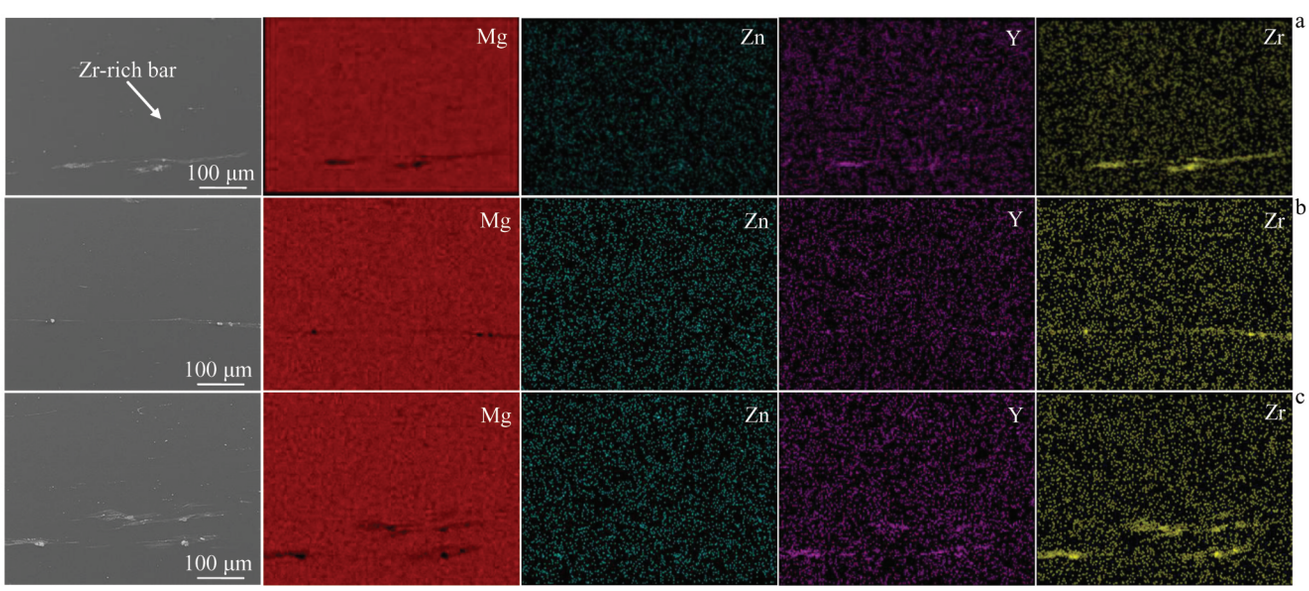

Fig.4 SEM images and EDS mappings of as-extruded ZWK210 alloys: (a) E440, (b) E460, and (c) E500

30~35 nm are also observed, as shown in Fig. 6f. The nano-sized long-rod-like second phase is parallel to the ED, which can be precipitated during the extrusion cooling.

2.2 Mechanical properties

Fig. 7a~7c show the SEM morphologies of tensile fracture of the as-extruded samples. The corresponding tensile properties of samples are summarized in Fig. 7d. Due to the low degree of dynamic recrystallization, E440 sample has obvious bimodal structure and poor tensile properties. The fracture surface is mainly composed of cleavage steps and slight dimples. The E460 exhibits excellent mechanical property, whose ultimate tensile strength (UTS), yield strength (YS) and elongation (EL) reach 317.1±5.5 MPa, 293.9±4.9 MPa and 16.7±1.5%, respectively. There is no significant difference in fracture morphology between E440 and E460 samples. As the extrusion temperature further increases, some DRXed grains in the alloy grow, and the strength of the E500 sample decreases, but its EL increases significantly, and relatively maintains a better value. There are many tiny dimples at the fracture of E500, which corresponds to the higher elongation.

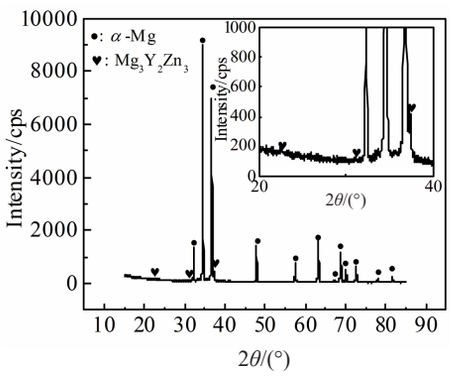

Fig.5 XRD pattern of E460 sample

2.3 Corrosion test

Fig.8 shows surface morphology and XRD pattern of E460 sample with corrosion products. The corrosion products uniformly cover the surface, which acts as a temporary protective layer to retard further corrosion. The XRD pattern shows that the corrosion products formed on the surface of E460 sample are mainly $Mg(OH)_2$ and $Ca_{10}(PO_4)_6(OH)_2$.

Fig.9 shows the results of mass loss (removal of corrosion products) and corrosion morphology of the alloy after immersion in SBF at 37 °C for 120 h. E460 has a low corrosion rate (0.669±0.017 mm·a^{-1}), good corrosion resistance, and relatively uniform corrosion morphology. In the E440 sample, there are small corrosion pits distributed along the ED band (Fig. 9a). The second phase particles are mainly concentrated in the compression zone (Fig. 4). The second phase particles keep a higher electric potential and form a potential difference with the α-Mg matrix in the SBF solution, thereby accelerating the dissolution of α-Mg. This indicates that the corrosion of the E440 sample preferentially starts from the second phase particles in the band-shaped region. The E460 sample has fine DRX grains and a relatively uniform microstructure, so its corrosion is relatively uniform. Some DRX grains in the E500 sample grow significantly (Fig. 3c), and the second phase particles rich in Zr and Y elements are segregated (Fig. 4c). A considerable number of corrosion pits are found on the corrosion surface of the E500 sample, and local corrosion occurs in some places (Fig.9c).

To further investigate the corrosion, three-dimensional corrosion morphologies (removal of corrosion products) are presented in Fig. 10. The E460 sample shows relatively uniform corrosion morphology (Fig. 10b). The lower the surface roughness (S_a) and line roughness (R_a) values, the better the corrosion resistance[4,5,15]. The S_a values of E440, E460 and E500 samples are 5.9, 4.5 and 12.6 μm, respectively. The R_a of the local corrosion area of E440, E460 and E500 samples are 5.7, 4.7 and 10.6 μm, respectively. The S_a and R_a values of the E460 sample are relatively low. Corrosion resistance is ranked according to strength: E460> E440> E500, which corresponds to the mass loss test.

Fig. 11 shows Nyquist plots and equivalent circuit of as-extruded alloys after immersion in SBF for 1 h. The E460 sample has a larger diameter of the capacitive loop, suggesting a better corrosion performance[31,32]. Fig. 11b shows the equivalent circuit. Table 1 exhibits the fitting data got from the EIS. R_s is the solution resistance. The constant phase element CPE_1 represents the electric double-layer capacity between the substrate and corrosion products film. R_p is the resistance of corrosion products film. R_{ct} represents charge transfer resistance. CPE_2 corresponds to the electric double-layer capacitance between the charge transfer resistance and the electrolyte solution. The value of R_{ct} has a close relationship with the corrosion resistance[20]. The higher the R_{ct} value, the better the corrosion resistance of the alloy. The E460 sample has a higher R_{ct}, showing a better corrosion resistance.

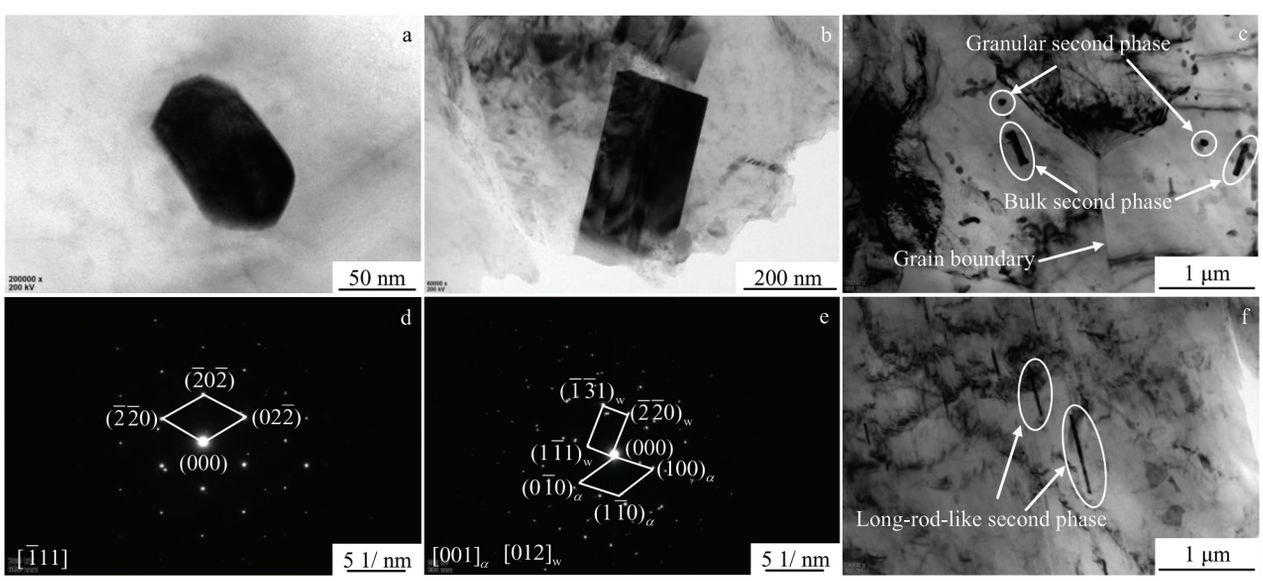

Fig.6 Bright field TEM images (a~c, f) of E460 sample and corresponding SAED patterns (d, e): (a, d) granular second phase, (b, e) bulk second phase, (c) grain boundary, and (f) long-rod-like second phase

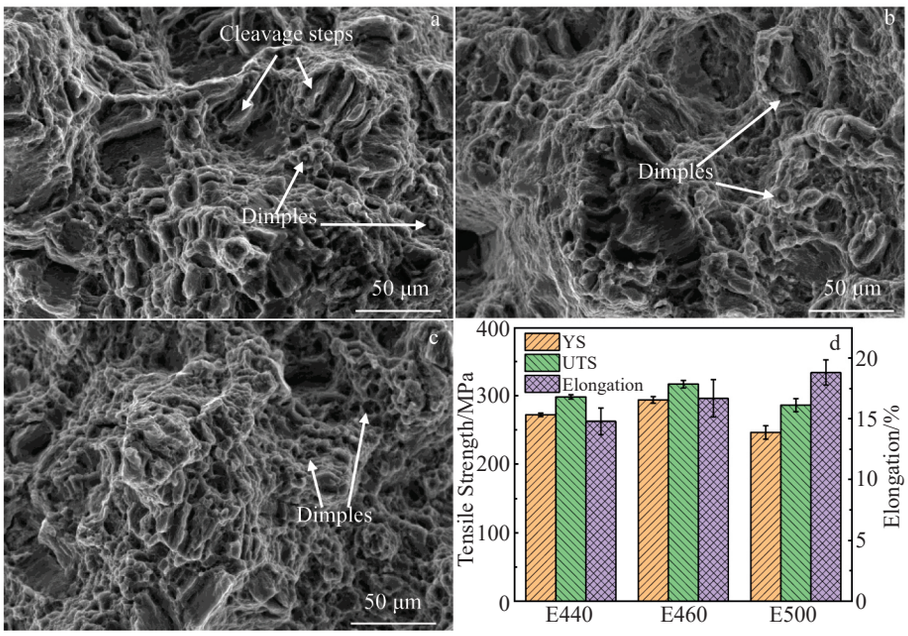

Fig.7 SEM images of fracture morphology of E440 (a), E460 (b) and E500 (c) samples and their tensile properties (d)

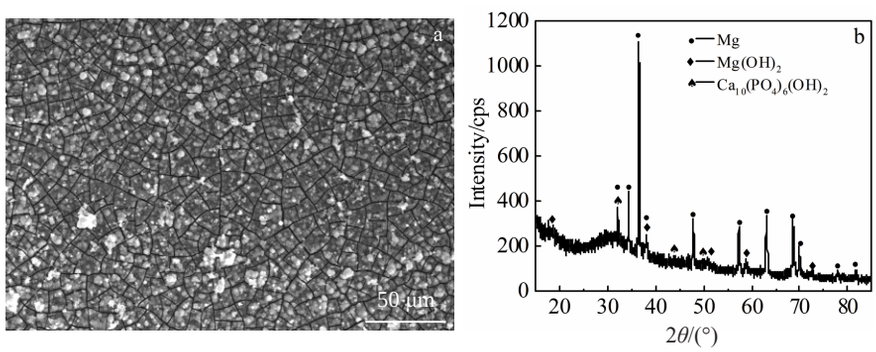

Fig.8 Surface morphology (a) and XRD pattern (b) of E460 sample after immersing in SBF solution for 120 h

Fig. 12 displays the polarization curves of as-extruded alloys after immersion in SBF for 1 h. The anode part of all polarization curves has a long passivation stage, indicating that there is a protective film on the sample surface[14]. The corrosion potential (E_{corr}), corrosion current density (I_{corr}) and breakdown potential (E_b) obtained from the polarization curves are shown in Table 2. The E460 sample possesses a relatively positive E_b (-1.290 V/SCE) and a smaller I_{corr} (3.151 μA·cm^{-2}), showing a good corrosion resistance.

3 Discussion

Extrusion temperature has a significant influence on dynamic recrystallization, texture, tensile properties and corrosion behavior[33,34]. In this work, some residual Y-rich and Zr-rich particles are observed in homogenized ZWK210 alloys (Fig. 1b). After extrusion, some concentrated Y-rich and Zr-rich particles are observed along the ED (Fig. 4). TEM analysis shows that the particles are $Mg_3Y_2Zn_3$ and Zn_2Zr phases. Partial dynamic recrystallization occurs at low temperature, showing bimodal structure with fine DRXed grains and elongated unDRXed grains (Fig. 2a). Shahzad et al[35] also reported the similar mixed grain structure and found that the Zr-rich cores are elongated to form either the fine grains, or elongated unDRX grains. Ji et al[36] also confirmed that the distribution of Zr is the reason for the formation of mixed grain structure of ZWK401 alloy during extrusion. Hu et al[37] also reported this phenomenon. They found that no recrystallization occurs at a low extrusion temperature near the Zr-rich bar region. There are two different morphologies in E440 sample around the densely distributed second-phase particles (Fig. 3a). One is the coarse unDRXed region for the segregation of the second-phase particles, and the other is the fine DRXed region formed by the pinning effect of some particles around the unDRXed region.

Fig. 13a~13c show the recrystallized fraction (RF) maps of as-extruded alloys. The unDRXed region of E440 sample is mainly composed of a few substructured grains and considerable deformed grains. The E440 sample presents high

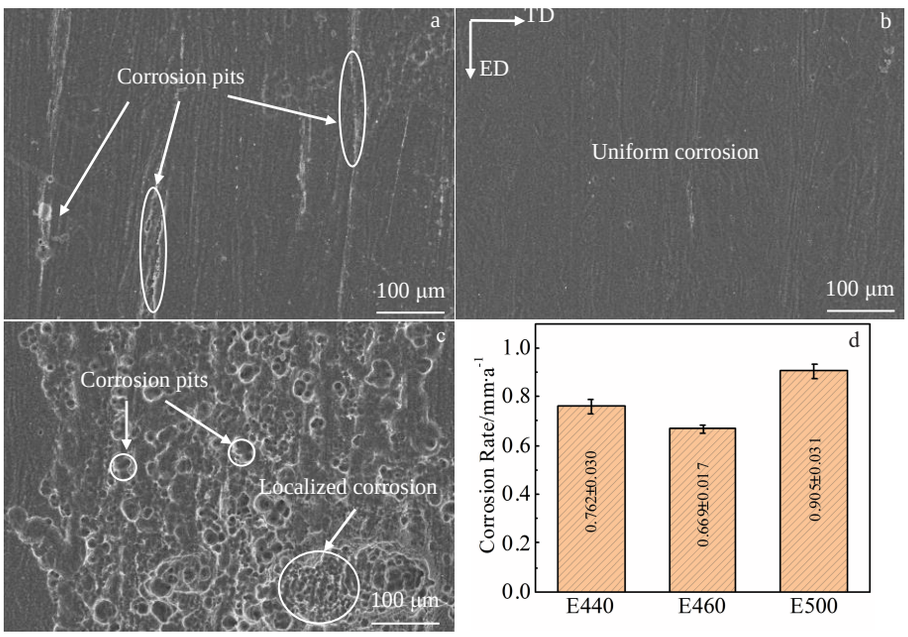

Fig.9 SEM images of the corrosion morphologies of E440 (a), E460 (b) and E500 (c) alloys and corresponding corrosion rate (d)

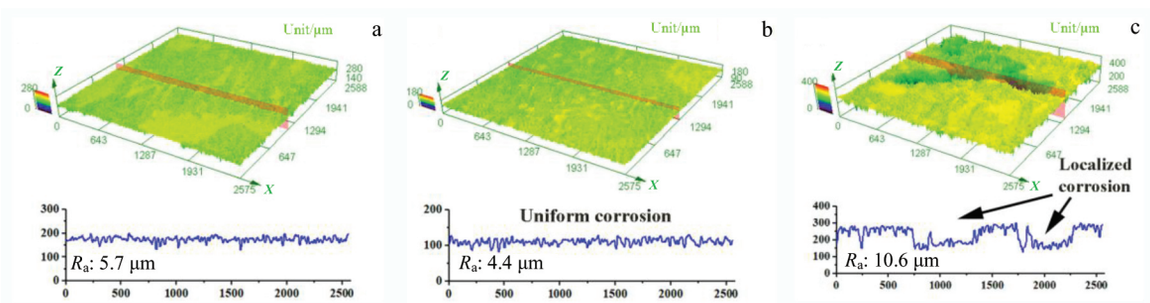

Fig.10 Three-dimensional corrosion morphologies of as-extruded alloys after removing corrosion products: (a) E440, (b) E460, and (c) E500

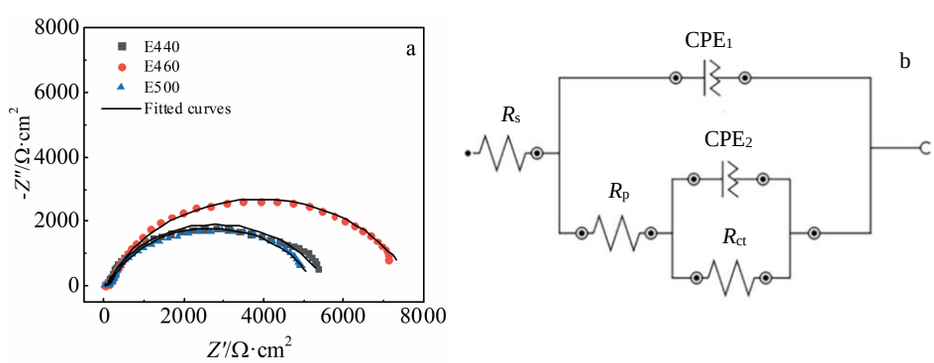

Fig.11 Nyquist plots (a) and equivalent circuit (b) of as-extruded alloys after immersion in SBF for 1 h

texture strength due to the bimodal structure. Through the analysis of texture component A (Fig. 3d), we find that high texture strength of E440 sample comes from coarse unDRXed grains (Fig. 3g). Combined with RF map (Fig. 13a), the deformed grains from unDRXed region contribute the most to the texture strength. The E460 sample shows relatively uniform DRXed grains with low texture strength. For RE-containing Mg alloys, DRXed grains with random orientation can weaken the texture strength[18]. Through the analysis of texture component B (Fig. 3e) and RF map (Fig. 13b), the

Table 1 Fitting results obtained from the EIS

Sample	R_s/Ω·cm^2	CEP$_1$/×10^{-5} F·cm^2	n_1	R_p/Ω·cm^2	CEP$_2$/×10^{-5} F·cm^2	n_2	R_{ct}/Ω·cm^2
E440	15.10	1.390	0.6528	98.41	1.612	0.8307	5493
E460	24.35	0.9795	0.6986	163.6	1.447	0.8215	7547
E500	20.56	1.378	0.6701	140.1	1.446	0.8328	5093

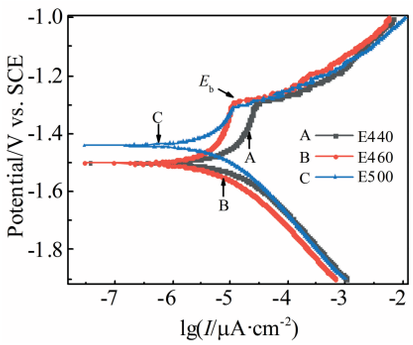

Fig. 12 Polarization curves of as-extruded alloys after immersion in SBF for 1 h.

Table 2 E_{corr}, I_{corr} and E_b obtained from the polarization curves

Sample	E_{corr}/V vs. SCE	I_{corr}/μA·cm^{-2}	E_b/V vs. SCE
E440	-1.501	5.525	-1.295
E460	-1.485	3.151	-1.290
E500	-1.441	5.483	-1.308

texture strength of E460 sample mainly comes from substructured grains and deformed grains (Fig. 3h). With further increasing the extrusion temperature, some DRXed grains grow obviously in E500 sample. Although unDRXed areas are observed due to selection problem, the corresponding EBSD maps can explain the problems related to the E500 sample to some extent. According to the analysis of texture component C (Fig. 3f) and RF map (Fig. 13c), the relatively high texture strength of E500 sample mainly comes from coarse unDRXed grains and a small part of the grown DRXed grains (Fig. 3i). This suggests that the grown DRXed grains can strengthen the texture strength. The bimodal structure with strong texture of E440 sample will cause local stress concentration and crack during the stretching process. Such non-uniform structure is the principal factor for the poor mechanical properties of E440 sample. The E460 sample with fine DRXed grains reveals a dominance of fine grain strengthening, showing excellent tensile properties. At higher extrusion temperature, the E500 sample shows relatively poor tensile properties. The decline of strength and the improvement of elongation of E500 sample are attributed to the subsequent growth of some DRXed grains[32].

Fig. 13d~13f show the kernel average orientation (KAM) maps of as-extruded alloys. The KAM maps show that unDRXed region has higher dislocation density than DRXed region. The unDRXed region has greater activity during the immersion, so it will give priority to the reaction with the SBF solution. In addition, the segregated particles around the unDRXed region will also cause the region to react preferentially with chloride ions in the solution. Thus, the E460 sample with lower dislocation density has good corrosion resistance in SBF. In addition, grain size and

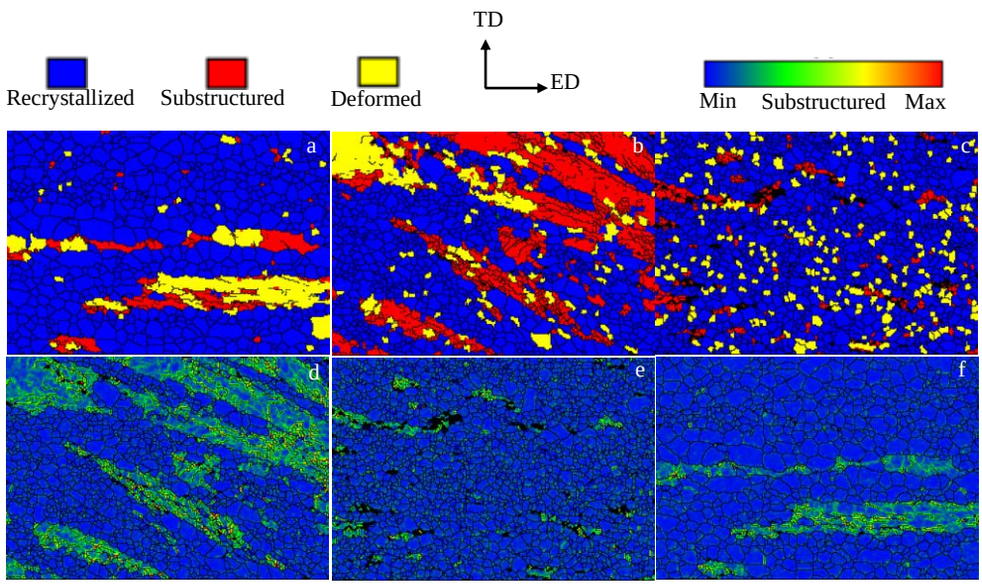

Fig.13 Recrystallized fraction (RF) maps (a~c) and kernel average misorientation (KAM) maps (d~f) of different alloys: (a, d) E440, (b, e) E460, and (c, f) E500

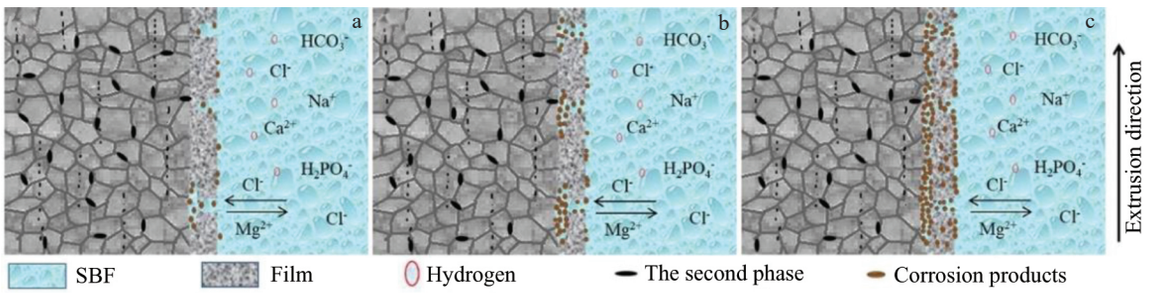

Fig.14 Schematic diagram of the corrosion mechanism of E460 sample in SBF: (a) first stage, (b) second stage, and (c) third stage

microstructure uniformity also affect the corrosion of Mg alloys. Fine-grained alloys have more grain boundaries than coarse-grained alloys. Kutniy et al[38] considered that the alloys with fine-grained microstructure have higher corrosion rates than the coarse-grained material. Song et al [39] found that grain boundaries will speed up the corrosion rate. However, Aung et al[19] reveals that during corrosion process, grain boundaries can retard the corrosion. Previous studies show that the passivation oxide film rapidly formed at the fine grain boundary of Mg alloys can hinder the development of corrosion. Xu et al[40] considered that the influence of grain boundary on corrosion should be discussed according to the properties of the corrosion system. In this study, all the polarization curves have an obvious passivation zone in the anode part (Fig.12), indicating that a protective film exists on the sample surface. For Mg alloys containing Y, a dense and continued Y_2O_3 protective film is easily formed on the surface[14,15]. For Mg alloys with fine grains, it is easier to form a protective oxide film at grain boundaries. The E440 sample exhibits a bimodal structure. It is easy to form uneven oxide film for the uneven structure. During immersion, weak part of the oxide film will be preferentially corroded to form the active sites. Besides, the unDRXed region with high dislocation density and concentrated particles will also have an adverse effect on the corrosion resistance of alloys. The E460 sample has uniform fine DRXed grains compared with the E440 sample. The considerable grain boundaries provide more nucleation sites for the dense oxide film[20]. In addition, the E460 sample has lower local internal stress according the corresponding KAM map. Thus, the E460 sample shows relatively uniform corrosion morphology (Fig.10b). The E500 sample shows relatively poor corrosion properties because of the uneven microstructure caused by the subsequent growth of some DRXed grains. Generally speaking, grain size, local internal stress and microstructure uniformity are the chief factors affecting the corrosion resistance for the investigated alloys.

Fig. 14 illustrates the schematic diagram of the corrosion mechanism of E460 sample in SBF solution. The E460 sample exhibits a uniform corrosion mode. In SBF solution, chloride ions will firstly erode the weak position between the oxide film and α-Mg matrix to form active sites (Fig. 14a). In addition, the second phase with a higher potential acts as the cathode and the α-Mg matrix acts as the anode in SBF. The uniformly distributed second phase provides a relatively uniform active site for the corrosion of the alloy. When the α-Mg matrix in contact with the weak part of the oxide film is preferentially dissolved in SBF solution, a lot of micro-galvanic corrosion will occur (Fig. 14b). As the immersion proceeds, the corrosion products are uniformly covered on the surface, which act as a temporary protective layer to retard further corrosion (Fig.14c).

4 Conclusions

1) The E440 sample shows a bimodal structure with coarse unDRXed grains and fine DRXed grains. The deformed grains from unDRXed region contribute the most to the texture strength. The E460 sample with uniform DRXed grains shows low texture strength. The grown DRXed grains of E500 sample can enhance the texture strength.

2) The E460 sample with fine DRXed grains reveals a dominance of fine grain strengthening, showing excellent tensile properties. However, due to the growth of some DRXd crystal grains, the tensile properties of the E500 sample are relatively poor.

3) E460 sample presents relatively good corrosion resistance, the corrosion rate is 0.669±0.017 $mm \cdot a^{-1}$, and the surface corrosion is relatively uniform. Grain size, recrystallization and microstructure uniformity are the principal factors affecting the properties of the investigated alloys.

References

1 Chen Y G, Xu Z G, Smith C *et al*. *Acta Biomater*[J], 2014, 10(11): 4561

2 Li H, Wen J B, He J G *et al*. *Advanced Engineering Materials*[J], 2020, 22: 1 901 360

3 Ding Y F, Wen C E, Hodgson P *et al*. *J Mater Chem B*[J], 2014, 2: 1912

4 Cai C H, Song R B, Li J Y. *Surf Coat Technol*[J], 2018, 342: 57

5 Chen J X, Tan L L, Yu X M *et al*. *J Mater Sci Technol*[J], 2019, 35: 503

6 Zhang X B, Yuan G Y, Wang Z Z. *Materials Science and Technology*[J], 2013, 29(1): 111

7 Ascencio M, Pekguleryuz M, Omanovic S. *Corros Sci*[J], 2014, 87: 489

8 Jafari H, Rahimi F, Sheikhsofla Z. *Mater Corros*[J], 2016,

67: 396
9 Gui Z Z, Kang Z X, Li Y Y. *J Alloy Compd*[J], 2016, 685: 222
10 Chen J X, Tan L L, Iniobong P E *et al*. *Mater Technol*[J], 2018, 33: 659
11 Zhang E L, Yin D S, Xu L P *et al*. *Mater Sci Eng C*[J], 2009, 29: 987
12 Wang J F, Li Y, Huang S *et al*. *J Mater Sci Technol*[J], 2014, 30: 1255
13 Fan J, Qiu X, Niu X D *et al*. *Mater Sci Eng C*[J], 2013, 33(4): 2345
14 He W W, Zhang E L, Yang K. *Mater Sci Eng C*[J], 2010, 30: 167
15 Liu Y, Wen J B, He J G *et al*. *J Mater Sci*[J], 2019, 55: 1813
16 Imandoust A, Barrett C D, Al-Samman T *et al*. *Journal of Materials Science*[J], 2016, 52: 1
17 Griffiths D. *Mater Sci Technol*[J], 2015, 31: 10
18 Guan D K, Mark Rainforth W, Le Ma *et al*. *Acta Mater*[J], 2017, 126: 132
19 Aung N N, Zhou W. *Corros Sci*[J], 2010, 52: 589
20 Xu Y Z, Li J Y, Qi M F *et al*. *J Mater Sci*[J], 2020, 55: 1231
21 Mostaed E, Hashempour M, Fabrizi A *et al*. *J Mech Behav Biomed Mater*[J], 2014, 37: 307
22 Zhang X B, Yuan G Y, Mao L *et al. J Mech Behav Biomed Mater* [J], 2012, 7: 77
23 Yao H, Wen J B, Xiong Y *et al*. *Rare Metal Material and Engineering*[J], 2019, 48(6): 1982 (in Chinese)
24 Wen J B, Lei S F, Liu Y *et al*. *Transactions of Materials and Heat Treatment*[J], 2017, 38(6): 67
25 Shi L, Min Z Y, He J G *et al*. *The Chinese Journal of Nonferrous Metals*[J], 2019, 29(6): 1161
26 Xu D Z, He J G, Wen J B *et al*. *Mater Res Express*[J], 2019, 6: 12
27 Lu Y, Bradshaw A R, Chiu Y L *et al*. *Mater Sci Eng C*[J], 2015, 48: 480
28 Zhang X B, Wu Y J, Xue Y J. *Materials Letters*[J], 2012, 86: 42
29 Bhattacharyya J J, Agnew S R, Muralidharan G. *Acta Materialia* [J], 2015, 86: 80
30 Guan D K, Mark Rainforth W, Gao J H. *Acta Mater*[J], 2018, 145: 399
31 Zander D, Zumdick N A. *Corrosion Science*[J], 2015, 93: 222
32 Ge M Z, Xiang J Y, Yang L. *Surface & Coatings Technology*[J] 2017, 310: 157
33 Liang J M, Guo X Q, Zheng Y F. *Journal of Materials Processing Technology*[J], 2016, 232: 78
34 Dai S, Wang F, Wang Z *et al*. *J Mater Sci*[J], 2020, 55: 375
35 Shahzad M, Wagner L. *Scr Mater*[J], 2009, 60: 536
36 Ji D W, Liu C M, Tang L C *et al*. *Mater Des*[J], 2014, 53: 602
37 Hu L F, Gu Q F, Li Q *et al*. *J Alloy Compd*[J], 2018, 741: 1222
38 Kutniy K V, Papirov I I, Tikhonovsky M A *et al*. *Material-wissenschaft und Werkstofftechnik*[J], 2009, 40: 242
39 Song G G, Xu Z Q. *Electrochim Acta*[J], 2010, 55: 4148
40 Xu H, Zhang X, Zhang K *et al*. *J Rare Earths*[J], 2016, 34: 315

挤压态生物可降解镁合金 Mg-2Zn-1Y-0.5Zr 的显微组织、力学性能和腐蚀行为

贺俊光[1,2]，徐大召[2]，文九巴[1,2]，师慧娜[1]，王扬帆[3]，任晓磊[4]
(1. 河南科技大学 材料科学与工程学院，河南 洛阳 471023)
(2. 有色金属协同创新中心，河南 洛阳 471023)
(3. 温州大学，浙江 温州 325000)
(4. 大连理工大学，辽宁 大连 116024)

摘　要：研究了挤压温度对挤压态Mg-2Zn-1Y-0.5Zr生物可降解镁合金动态再结晶、织构和拉伸性能的影响，基于显微组织和腐蚀形态阐述了挤压态合金在模拟体液中的腐蚀机理。结果表明，在440 ℃（E440）下挤压的合金出现双峰结构，具有粗大的未再结晶（unDRXed）晶粒和细小的再结晶（DRXed）晶粒。未再结晶区域的变形晶粒对织构强度的影响最大。460 ℃的挤压合金（E460）具有均匀的再结晶晶粒，晶粒细化后拉伸性能显著改善。同时，均匀的再结晶晶粒会弱化织构强度。E460的样品表现出最佳耐腐蚀性，腐蚀速率为0.669±0.017 mm·a^{-1}。

关键词：生物可降解；挤压；再结晶；腐蚀行为

作者简介：贺俊光，女，1970年生，博士，副教授，河南科技大学材料科学与工程学院，河南 洛阳 471023，E-mail：he.ellen@163.com